J. Fluid Mech. (1995), vol. 292, pp. 71–94

The motion of long bubbles in polygonal capillaries. Part 1. Thin films

By HARRIS WONG,[1]† C. J. RADKE[2] AND S. MORRIS[1]

[1] Department of Mechanical Engineering, University of California, Berkeley, CA 94720, USA

[2] Earth Sciences Division of Lawrence Berkeley Laboratory and Department of Chemical Engineering, University of California, Berkeley, CA 94720, USA

(Received 22 January 1993 and in revised form 26 September 1994)

Foam in porous media exhibits an unusually high apparent viscosity, making it useful in many industrial processes. The rheology of foam, however, is complex and not well understood. Previous pore-level models of foam are based primarily on studies of bubble flow in circular capillaries. A circular capillary, however, lacks the corners that characterize the geometry of the pores. We study the pressure–velocity relation of bubble flow in polygonal capillaries. A long bubble in a polygonal capillary acts as a leaky piston. The 'piston' is reluctant to move because of a large drag exerted by the capillary sidewalls. The liquid in the capillary therefore bypasses the bubble through the leaky corners at a speed an order higher than that of the bubble. Consequently, the pressure work is dissipated predominantly by the motion of the fluid and not by the motion of the bubble. This is opposite to the conclusion based on bubble flow in circular capillaries. The discovery of this new flow regime reconciles two groups of contradictory foam-flow experiments.

Part 1 of this work studies the fluid films deposited on capillary walls in the limit $Ca \rightarrow 0$ ($Ca \equiv \mu U/\sigma$, where μ is the fluid viscosity, U the bubble velocity, and σ the surface tension). Part 2 (Wong *et al.* 1995) uses the film profile at the back end to calculate the drag of the bubble. Since the bubble length is arbitrary, the film profile is determined here as a general function of the dimensionless downstream distance x. For $1 \ll x \ll Ca^{-1}$, the film profile is frozen with a thickness of order $Ca^{2/3}$ at the centre and order Ca at the sides. For $x \sim Ca^{-1}$, surface tension rearranges the film at the centre into a parabolic shape while the film at the sides thins to order $Ca^{4/3}$. For $x \gg Ca^{-1}$, the film is still parabolic, but the height decreases as film fluid leaks through the side constrictions. For $x \sim Ca^{-5/3}$, the height of the parabola is order $Ca^{2/3}$. Finally, for $x \gg Ca^{-5/3}$, the height decreases as $Ca^{1/4}x^{-1/4}$.

1. Introduction

Foam in porous media consists of gas bubbles dispersed in a surfactant solution. Most bubbles are larger than the typical pore dimensions (Chambers & Radke 1990). Interaction between long bubbles and pore walls gives foam a yield stress and a shear-thinning behaviour (Assar & Burley 1986). The interaction also gives foam an apparent viscosity that can be 100 times that of the liquid constituent (Falls, Musters & Ratulowski 1989). The resulting low mobility makes foam appealing as a displacing agent in oil recovery (Holm & Garrison 1988; Hirasaki 1989) and as a sealant in underground natural gas reservoirs (Albrecht & Marsden 1970).

---

† Present address: The Levich Institute, The City College of CUNY, New York, NY 10031, USA.

Understanding of the complex rheology of foam must start from the pore level. The simplest model of the irregular pores in porous media is a straight tube of circular section. Bubble flow in circular tubes was first studied in the limit $Ca \rightarrow 0$ by Bretherton (1961). He found that the pressure drop needed to move a long bubble scales as $Ca^{2/3}$. This is an order larger than the pressure drop ($\sim Ca$) needed to drive a unit column of fluid, and seems to explain the high apparent viscosity and shear-shinning behaviour of foam. Consequently, the $\frac{2}{3}$ scaling has been incorporated widely into pore-level models of foam (Kovscek & Radke 1994).

Recently, several foam-flow experiments at low flow rates revealed that the pressure drop over a porous core varies linearly with liquid flow, but is insensitive to gas flow (Kovscek & Radke 1994; and references therein). None of the existing theories based on circular-tube results can predict this behaviour.

This work studies the pressure–velocity relation of bubble flow in polygonal capillaries. A long bubble in a polygonal capillary acts as a leaky piston. The leaky corners have the same order of cross-sectional area as the capillary. Thus, the liquid in the capillary can bypass the bubble through corner channels (corner flow). In addition, the liquid also flows by pushing the bubble (plug flow). The ratio of corner to plug flow depends on the liquid flow rate. At moderately low flow rates, the plug flow dominates, and it obeys the $\frac{2}{3}$ scaling as in circular capillaries. However, at extremely low liquid flow rates, the corner flow dominates and yields a linear relation of liquid pressure gradient versus liquid flow. In this linear regime, the bubble motion dissipates insignificant amount of mechanical energy, and therefore has no effect on the pressure gradient. The linear relation and its insensitivity to bubble motion provide an explanation for the peculiar foam-flow behaviour at low flow rates.

In plug flow, the liquid pushes the bubble. A moving long bubble in a polygonal capillary deposits liquid films on the capillary walls. The thickness of the films is an order smaller than the width of the capillary. Hence, the pressure work driving the plug flow is dissipated predominantly in the films. The main purpose of Part 1 is to determine the film profile so that the dissipation can be calculated.

Flow of clean bubbles in circular capillaries has been thoroughly explored (see, for example, Schwartz, Princen & Kiss 1986). Therefore, it is a useful prototype for studying film profiles in polygonal capillaries. In the limit $Ca \rightarrow 0$, a long bubble in a circular capillary can be divided into outer cap regions where surface tension dominates and inner film regions where viscous and surface tension forces are equally important (Bretherton 1961). The deposited fluid film is of order $Ca^{2/3}$ in thickness. Dissipation of mechanical energy is strongest in the inner regions at the front and back of the film. These regions determine the pressure drop needed to move the bubble because the total dissipation equals the rate of pressure work. Between the ends, the film is uniform. Owing to the lack of film rearrangement, the length of a clean bubble plays no part in the solution. This is not true for bubbles in polygonal capillaries.

The same basic inner and outer structure exists for long bubbles in polygonal capillaries in the limit $Ca \rightarrow 0$, as sketched in figure 1. The mathematical model to be solved is stated in §2. Section 3 describes the outer solution. This is a static meniscus intersecting the walls in apparent contact lines, as illustrated in figure 1. The inner solution gives a high-resolution view of the apparent contact line, and of the thin film deposited by it. Throughout the inner region, the meniscus is nearly parallel to the wall and the lubrication approximation holds. Section 4 uses this approximation to derive the (partial-differential) equation governing the film thickness throughout the inner region. Simplification of this equation is possible in six subregions of the inner region. Thus, §5 describes the flow within the apparent contact line. This region is essential to

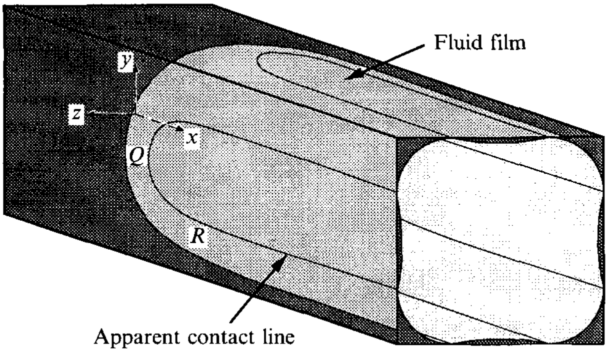

FIGURE 1. Front half of a long bubble (light shading) flowing through a wetting liquid (dark shading) in a square capillary. A coordinate system is fixed at the nose of the bubble. The diagram also shows apparent contact lines and thin films. The thickness of the fluid films is exaggerated for illustrative purposes.

understanding how the liquid moves the bubble. As in the axisymmetric flow studied by Bretherton (1961), in the limit $Ca \rightarrow 0$, dissipation of mechanical energy due to the motion of the bubble is essentially confined to the apparent contact region. However, the structure of this region now differs in one essential form from that in the axisymmetric flow. We show that the film thickness at the front contact region changes from $O(Ca^{2/3})$ at the leading edge (Q in figure 1) to $O(Ca)$ along the section (R in figure 1) parallel to the direction of bubble motion. This variation in thickness means that surface tension rearranges the film in the downstream direction. Therefore, the structure of the trailing contact region depends on the bubble length, and so does the pressure drop needed to move the bubble at a given velocity. As noted at the end of the previous paragraph, this is an essential difference between the present flow and the axisymmetric flow. Sections 6 and 7 describe the evolution of the film. Specifically, the film thickness seen by the trailing bubble cap is given by (6.10) or (7.7) depending on bubble length. Section 8 shows how this initial profile influences the trailing contact region. Part 2 of this paper uses these results to find the relation between liquid flow rate and bubble velocity.

Film profiles derived in this paper also apply to bubbles in Hele-Shaw cells: rectangular capillaries with high aspect ratio. When a non-wetting fluid is injected into a Hele-Shaw cell initially filled with a wetting, more viscous liquid, the fluid advances in the shape of a finger and deposits a liquid film on the wall (Saffman & Taylor 1958). The deposition process has been analysed theoretically by Park & Homsy (1984) and Reinelt (1987). However, they did not solve the subsequent film rearrangement. Recently, Burgess & Foster (1990) studied theoretically the motion of a flat circular gas bubble through a Hele-Shaw cell. They analyse the termination of the film. However, a circular flat bubble is not long enough for the film to rearrange. Here, we study long bubbles where it is necessary to consider rearrangement. Results for polygonal capillaries also apply to Hele-Shaw cells because the inner limit of the outer solution is the same in both problems.

Although only clean bubbles are considered here, our solutions apply directly to surfactant-laden bubbles when the bubble surface is remobilized by the surfactant. Stebe, Lin & Maldarelli (1991) have shown both theoretically and experimentally that a surfactant-laden interface may mobilize when the bulk surfactant concentration is high enough to eliminate a diffusion boundary-layer resistance, and when the rate of surfactant adsorption and desorption is fast compared to the rate of convection of adsorbed surfactants along the surface. Under these conditions, the surfactant concentration is constant along the interface. The motion of a surfactant-laden bubble is then the same as that of a clean bubble, except that the surface tension is lower by a constant value everywhere on the interface.

2. Governing equations

Figure 1 illustrates the physical situation. The gas bubble moves with constant velocity U through a straight square capillary initially filled with a wetting Newtonian liquid of viscosity μ. The gas is taken as effectively inviscid and incompressible. The gas/liquid interface has a constant surface tension σ. The radius, a, of the largest inscribed sphere of the capillary is small, so that inertia and gravity effects can be neglected. The coordinates are fixed at the nose of the bubble with x pointing downstream, as shown in figure 1. Lengths, velocity, pressure, and force are made dimensionless using a, U, σ/a, and $a\sigma$, respectively.

The dimensionless momentum and continuity equations are

$$\tilde{\nabla} p = Ca\tilde{\nabla}^2 \tilde{\boldsymbol{u}}, \quad \tilde{\nabla}\cdot\tilde{\boldsymbol{u}} = 0, \tag{2.1a, b}$$

where $\tilde{\nabla} = \boldsymbol{i}\,\partial/\partial x + \boldsymbol{j}\,\partial/\partial y + \boldsymbol{k}\,\partial/\partial z$, p is the fluid pressure (the bubble pressure is set to zero), $Ca \equiv \mu U/\sigma$ is the capillary number, and $\tilde{\boldsymbol{u}} = u\boldsymbol{i} + v\boldsymbol{j} + w\boldsymbol{k}$ is the fluid velocity.

On the wall, no-slip requires that

$$\tilde{\boldsymbol{u}} = \boldsymbol{i}. \tag{2.1c}$$

Motion is assumed to be steady in the moving coordinates. The surface of the bubble is therefore a stream surface, so that at the gas/liquid interface

$$\boldsymbol{n}\cdot\tilde{\boldsymbol{u}} = 0. \tag{2.1d}$$

At the interface, the boundary condition on the stress is

$$(-p\boldsymbol{I} + 2Ca\boldsymbol{E})\cdot\boldsymbol{n} = \boldsymbol{n}\tilde{\nabla}\cdot\boldsymbol{n}. \tag{2.1e}$$

Here, $\boldsymbol{I}$ is the unit tensor, $\boldsymbol{E}$ is the strain rate tensor, $\boldsymbol{n}$ is the unit vector normal to the gas/liquid interface pointing from the gas towards the liquid, and $\tilde{\nabla}\cdot\boldsymbol{n}$ is the mean curvature of the interface (Weatherburn 1938, p. 131).

As mentioned in §1, in the limit $Ca\rightarrow 0$ the bubble in figure 1 can be divided into two regions: an outer region away from the wall where surface tension dominates and an inner region near the wall where surface tension and viscous forces are comparable. The viscous film thins continuously as $Ca\rightarrow 0$, but the limiting case of $Ca = 0$ is never reached because the topology of a moving bubble differs from that of the static bubble. Hence, the perturbation from the static state is singular, and a singular-perturbation method is used to determine the first-order effect of viscous forces.

3. Outer solution

The outer problem is obtained by applying the limit $Ca\rightarrow 0$ to the governing equations. In this limit, the momentum equation (2.1a) requires $\tilde{\nabla} p = 0$. The liquid pressure is therefore uniform or $p = -\alpha$ (constant). The stress boundary condition (2.1e) then becomes

$$\tilde{\nabla}\cdot\boldsymbol{n} = \alpha. \tag{3.1a}$$

Equation (3.1a) governs the shape of the static bubble. The constant α is the mean curvature of the bubble surface and is determined by an integral force balance

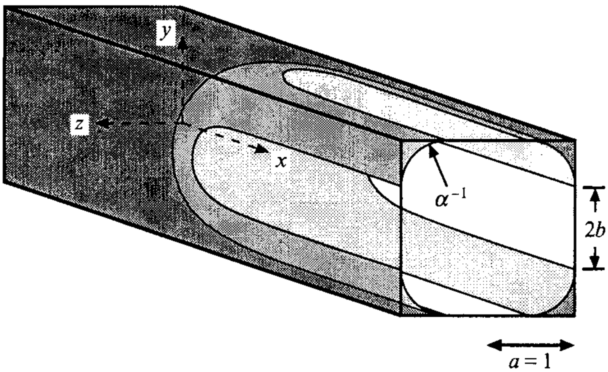

FIGURE 2. Half of a static long bubble in a square capillary. The meniscus far away from the nose reduces to circular arcs with radius $1/\alpha$.

Capillary shapes	α	b	c	x_0	A_0
$N = 3$	1.7776	0.75765	1.990	0.8549	0.1935
$N = 4$	1.8862	0.46984	3.274	0.8737	0.1136
$N = 6$	1.9523	0.28162	5.532	0.9059	0.06602
$B = 1.2$	1.7300				
shorter side		0.42195	3.094	1.050	0.1066
longer side		0.62195	2.878	0.8776	0.1702
$B = 1.5$	1.5759				
shorter side		0.36544	2.888	1.322	0.09526
longer side		0.86544	2.413	0.8868	0.2690
$B = 2$	1.4247				
shorter side		0.29810	2.637	1.786	0.07814
longer side		1.29810	1.860	0.9044	0.4597

α is the mean curvature calculated analytically from (A 3) and (A 6).
b is determined analytically from (A 2), (A 4) and (A 5).
A_0 is the scaled film area defined in (5.7).

TABLE 1. Fitting parameters c and x_0 of contact lines

(Appendix A). Table 1 lists the results for three regular-polygonal capillaries of N sides and three rectangular capillaries with aspect ratios B. The static bubble intercepts the wall at an apparent contact line because the trailing film is thin. The effective contact angle is zero because the slope of the meniscus in the trailing film vanishes in the limit $Ca \rightarrow 0$.

The boundary condition for (3.1 *a*) is therefore the matching condition

$$\boldsymbol{m} \cdot \boldsymbol{n} = 1, \tag{3.1b}$$

where $\boldsymbol{m}$ is a unit vector normal to the capillary wall.

Equation (3.1) defines a free-boundary problem because the contact line is not known in advance. The problem has been solved numerically for several polygonal capillaries by Wong, Morris & Radke (1992*b*). Two properties of the solutions are needed here for matching. First, in all the capillaries considered here, points (x, z) on the contact line satisfy the equation

$$\cos(\pi z/2b) = \exp(-c(x - x_0)), \tag{3.2}$$

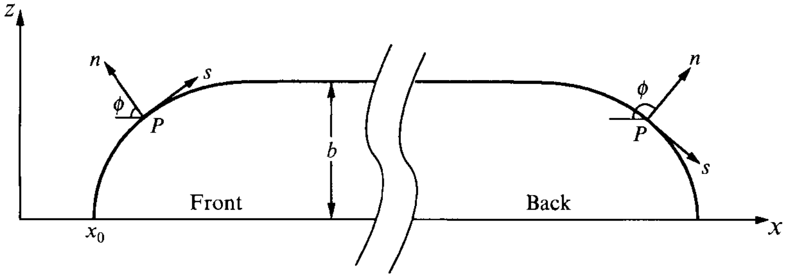

FIGURE 3. Definition sketch of the Cartesian coordinates (n,s) for the front and back ends. The origin P is a point on the contact line. Points (x,z) on the contact line obey (3.2).

where $2b$ is the separation between the two branches of the contact line at large x, as portrayed in figure 2. Table 1 lists the values of b determined from the meniscus geometry (Appendix A). The constants x_0 and c depend on the capillary; the values given in table 1 were obtained by fitting (3.2) to our numerical results (Wong 1992, p. 71). As written, (3.2) holds only for the front half of the contact line. (It holds for the back half when the obvious change in origin is made.) This explicit form for the contact line is used in calculating the deposition of the fluid film in §5.

Secondly, for matching, we also need the curvature of the static meniscus along the section normal to the contact line. Let h be the height of the meniscus above the wall. Let P be a point on the contact line, and introduce orthogonal Cartesian coordinates (n,s) with origin at P, and n normal to the contact line, as shown in figure 3. Because $\partial h/\partial n = 0 = \partial h/\partial s$ at P, (3.1) requires $\partial^2 h/\partial n^2 + \partial^2 h/\partial s^2 = \alpha$ at P, i.e. α is the sum of the curvatures in the n and s directions. However, $\partial^2 h/\partial s^2$ vanishes at P, and is non-zero away from P only if the contact line is curved. The interfacial curvature normal to the contact line therefore equals the mean curvature of the static meniscus at any point P on the contact line, i.e.

$$\frac{\partial^2 h}{\partial n^2} \to \alpha \quad \text{as } n \to 0. \tag{3.3}$$

This matching condition is applied to the flow in the viscous contact regions in §5 and §8. It is derived more rigorously by Wong (1992, p. 107), using the arc length along the contact line and the distance normal to the contact line as curvilinear coordinates.

4. Governing equation for the inner region

A moving long bubble in a capillary tube deposits a fluid film on the wall (figure 1). Within this thin film, the shear stresses are large enough to make the viscous term important in the momentum balance (2.1 a). Because the film proves to be nearly parallel to the wall, the lubrication approximation holds and is used in this section to derive the governing equation for the inner region.

Under the lubrication approximation, the momentum equation (2.1 a) becomes

$$\nabla p = Ca\frac{\partial^2 \boldsymbol{u}}{\partial y^2}, \quad \frac{\partial p}{\partial y} = 0, \tag{4.1 a,b}$$

where $\nabla = \boldsymbol{i}\,\partial/\partial x + \boldsymbol{k}\,\partial/\partial z$ and $\boldsymbol{u} = u\boldsymbol{i} + w\boldsymbol{k}$. (The film at $y = 1$ in figure 1 is used to demonstrate the derivation.) On the wall, the no-slip boundary condition requires that

$$\boldsymbol{u} = \boldsymbol{i} \quad \text{at} \quad y = 1. \tag{4.2}$$

The stress jump conditions at the interface simplify to

$$\frac{\partial \boldsymbol{u}}{\partial y} = 0, \quad p = -\nabla^2 h \quad \text{at } y = 1-h, \tag{4.3a,b}$$

where h is the height of the film to be determined.

Integration of the continuity equation (2.1 *b*) across the film shows that

$$\nabla \cdot \boldsymbol{q} = 0, \tag{4.4a}$$

where

$$\boldsymbol{q} \equiv \int_{1-h}^{1} \boldsymbol{u} \, \mathrm{d}y \tag{4.4b}$$

is the volume flow across a plane area normal to $\boldsymbol{u}$, with unit width and with height equal to the film thickness. The velocity $\boldsymbol{u}$ is found from (4.1) to (4.3) as

$$\boldsymbol{u} = \boldsymbol{i} + \frac{1}{Ca}[h(1-y) - \tfrac{1}{2}(1-y)^2]\, \nabla \nabla^2 h. \tag{4.5}$$

Substitution into (4.4 *b*) gives

$$\boldsymbol{q} = h\boldsymbol{i} + \frac{1}{3Ca} h^3 \nabla \nabla^2 h. \tag{4.6}$$

This equation shows the two contributions to the volume flux. The first is due to the motion of the wall, which sweeps fluid from the front of the bubble to the back. The second is due to the gradient in the capillary pressure, $p = -\nabla^2 h$, which sucks fluid from the film. At the front of the bubble, a balance between the two volume fluxes yields the thickness of the film. At the middle section of the bubble, the cross-stream pressure gradient, being unopposed, sucks fluid away from the film to form a severe constriction at the film boundary. At the back of the bubble, the pressure gradient tends to generate another severe constriction. However, the film carried by the wall supplies sufficient fluid to the constriction to prevent it from closing. The balance yields an oscillatory film profile.

The field equation for h is obtained from (4.4 *a*) as

$$\frac{\partial h}{\partial x} + \frac{1}{3Ca} \nabla \cdot (h^3 \nabla \nabla^2 h) = 0. \tag{4.7}$$

Equation (4.7) holds throughout the thin film because the lubrication analysis leading to it assumes only that the meniscus is nearly parallel to the wall. (The analysis of (4.7) given in § 5 shows the maximum slope within the film to be of order $Ca^{1/3}$, and that matching of the solution of (4.7) to the static meniscus is possible.)

Results of the six subregions of the film are first summarized here. Figure 4 shows the corresponding lengthscales. The film is deposited by the apparent contact line (region 1) of width $Ca^{1/3}$. In the downstream distance $x \sim 1$, the film thickness at the centre is $O(Ca^{2/3})$, and it decreases to $O(Ca)$ at the sides (region 2) before merging to the corner meniscus (figure 1). This initial film profile is frozen in $x \ll Ca^{-1}$. When $x \sim Ca^{-1}$, surface tension rearranges the film at the centre into a parabolic shape (region 3) while the film at the sides (region 4) thins to $O(Ca^{4/3})$. For $x \gg Ca^{-1}$, the film remains parabolic, but the height decreases as film fluid leaks through the sides (region 5). The trailing film of height h_1 terminates in a strip of width $h_1/Ca^{1/3}$ (region 6). The purpose of Part 1 is to determine $h_1(x, z)$.

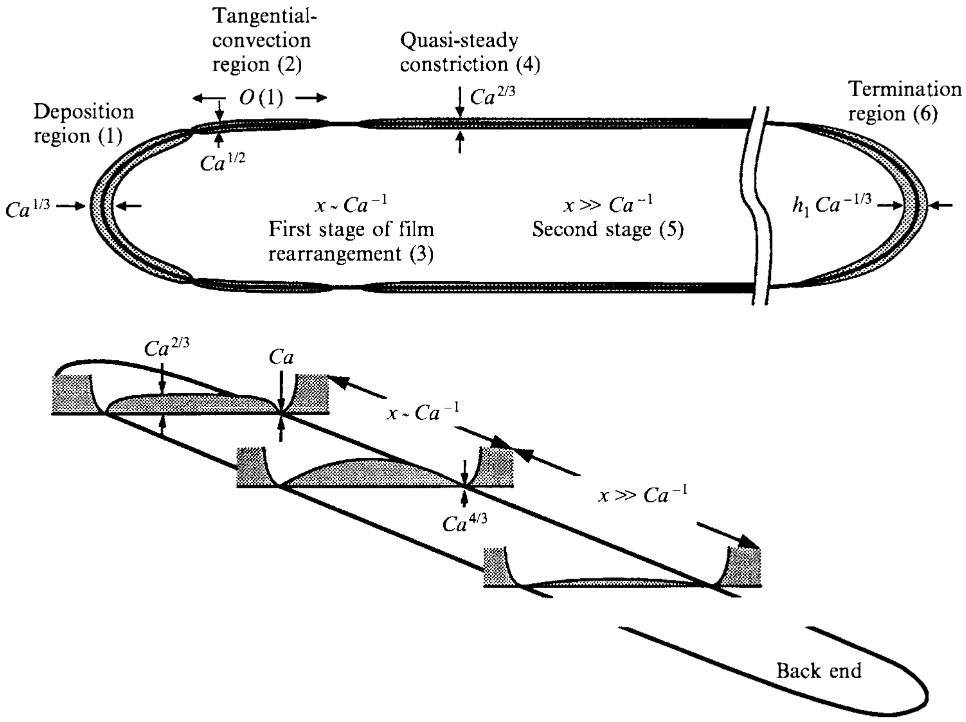

FIGURE 4. Lengthscales of the six film subregions. The static contact lines are depicted by thick lines. The top diagram shows the width and length of each region while the lower diagram illustrates the corresponding film profile and height. h_1 is the film height arriving at the back end. The slope of the film is small everywhere as indicated by the lengthscales. The film height is exaggerated for illustrative purposes.

5. Film deposition

The film is deposited by the apparent contact line sketched in figure 4. Dissipation of mechanical energy owing to the motion of the bubble is largest in the thin film. The pressure drop needed to displace the bubble is therefore determined by the motion within the film. For axisymmetric flow without surfactants, much of the film is static, and dissipation is confined to the contact region. We show this is true even when the flow is not axisymmetric.

In the limit $Ca \rightarrow 0$, the shape of the apparent contact line becomes independent of Ca, but the width of the contact region vanishes. This implies that the width of the region becomes small compared with the radius of curvature of the apparent contact line, and hence that local Cartesian coordinates can be used. In terms of the (n, s) coordinates in figure 3, (4.7) becomes

$$\frac{1}{3Ca}\frac{\partial}{\partial n}\left(h^3\frac{\partial^3 h}{\partial n^3}\right)-\frac{\partial h}{\partial n}\cos\phi+\frac{\partial h}{\partial s}\sin\phi = 0, \tag{5.1}$$

where the angle ϕ depends only on s, and is defined by the outer solution. The capillary-pressure gradient along the apparent contact line is order $(n/s)^3$ compared with that normal to it, and is therefore negligible because the width of the contact region is small compared with its length.

The second and third terms in (5.1) represent normal and tangential convection. Because $\partial/\partial s \sim 1$ and $\partial/\partial n \sim n^{-1}$, where $n \ll 1$, the ratio of normal to tangential convection is $\cos(\phi)/n \sin(\phi)$. This ratio is large compared with one, unless $\cos(\phi) \sim n$, i.e. if $\frac{1}{2}\pi - \phi \sim n$. Tangential convection is thus negligible in (5.1) except where the contact line is almost parallel to the direction of bubble motion. Outside this region, mass flow along the contact line is negligible, and (5.1) simplifies to

$$\frac{\partial q}{\partial n} = 0, \tag{5.2a}$$

where

$$q = \frac{1}{3Ca} h^3 \frac{\partial^3 h}{\partial n^3} - h \cos\phi. \tag{5.2b}$$

The volume flux has two contributions. One is due to the gradient in capillary pressure, which sucks fluid from the film. The other is due to the motion of the wall, which drags fluid into the film. From (5.2), the difference between the two fluxes must be constant along a section normal to the contact line. The difference is the volume flux (height) of the trailing film carried away by the wall. Integration of (5.2) gives

$$\frac{\partial^3 h}{\partial n^3} = 3Ca \cos(\phi) \frac{h - h_0}{h^3}, \tag{5.3}$$

where $h_0(s)$ is the thickness of the trailing film to be determined. Equation (5.3) is identical to the classical equation of Landau & Levich (1942) and Bretherton (1961) when the capillary number is redefined using the velocity component normal to the contact line. Thus, only a summary of the solution of (5.3) is presented here. Details are given in Appendix B. As $n \rightarrow \infty$, $h \rightarrow \infty$, and (5.3) requires $\partial^3 h/\partial n^3 \rightarrow 0$ or

$$\frac{\partial^2 h}{\partial n^2} \rightarrow \frac{k_1}{h_0} (3Ca \cos\phi)^{2/3}, \tag{5.4}$$

where $k_1 = 0.64304$ is determined by solving (5.3) numerically (Appendix B). This result is used to find $h_0(s)$.

The film thickness, h_0, is obtained by matching the normal curvatures in (3.3) and (5.4):

$$h_0 = \frac{k_1}{\alpha} (3Ca \cos\phi)^{2/3}. \tag{5.5}$$

$\phi(s)$ is a known function of s (or z), because the contact line is known from (3.2). Hence, for all capillaries described in table 1,

$$h_0(z) = \frac{k_1}{\alpha} (3Ca)^{2/3} \left[1 + \left(\frac{\pi}{2bc} \right)^2 \tan^2 \left(\frac{\pi z}{2b} \right) \right]^{-1/3}, \tag{5.6}$$

where α, b, and c depend on capillary shape. This film profile is plotted in figure 5 (solid line) for the square capillary. The scaled area

$$A_0 = \frac{1}{(3Ca)^{2/3}} \int_0^b h_0 \, \mathrm{d}z \tag{5.7}$$

is used to normalized $h_0(z)$. Table 1 lists the values of A_0 for various capillaries. The initial film profile $h_0(z)$ is maintained in the downstream distance $x \ll Ca^{-1}$.

Equation (5.6) gives $h_0(z = b) = 0$. This means that the film thickness at the sides of the film is zero to the order of $Ca^{2/3}$ or $h = o(Ca^{2/3})$. At the sides, $\cos\phi \rightarrow 0$, so the

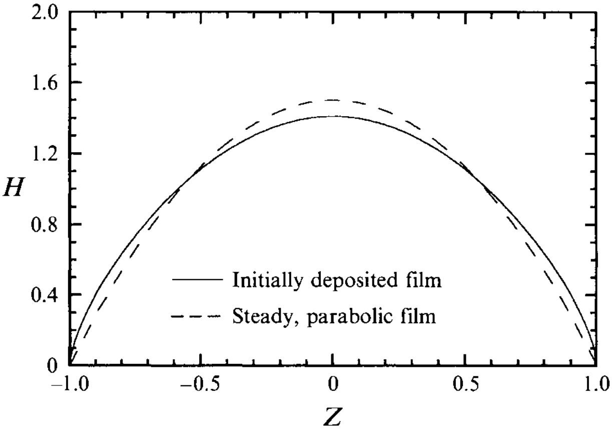

FIGURE 5. Film profiles in a square capillary. H and Z are normalized film height and cross-stream distance defined in (6.6). The area under the two curves is the same.

tangential-convection term in (5.1), which was neglected in the deposition region, becomes important. The effect of this term is studied in the next subsection.

5.1. *Tangential-convection region*

The tangential-convection region is located at the sides of the film, as depicted in figure 4. In this region, the normal component of convection, which drags fluid into the film, approaches zero, whereas the normal capillary suction, which sucks fluid away from the film, remains the same as that in the front. Thus, the film becomes much thinner than that at the front. Even though the film is thin, lateral fluid leakage caused by the capillary suction may be significant. The purpose of this section is to determine the amount of fluid sucked away from the film throughout the tangential-convection region, and to establish whether that leakage has any significant effect on the deposited film.

The film thickness in this region is governed by (5.1), i.e.

$$\frac{1}{3Ca}\frac{\partial}{\partial n}\left(h^3\frac{\partial^3 h}{\partial n^3}\right)-\frac{\partial h}{\partial n}\cos\phi+\frac{\partial h}{\partial s}\sin\phi=0.$$

Here, $\cos\phi \ll 1$, so normal convection has decreased to become comparable with tangential convection. Since we are interested in the leakage and not in the actual film profile, a scaling analysis is sufficient.

Lengthscales of the tangential-convection region are determined from the matching condition, the governing equation (5.1), and the geometry of the contact line. The matching condition in (3.3) states that

$$\frac{\partial^2 h}{\partial n^2}\sim 1. \tag{5.8}$$

Balancing dominant terms in (5.1) yields the following two equations:

$$h^3\frac{\partial^3 h}{\partial n^3}\sim Ca\,h\cos\phi, \tag{5.9}$$

and

$$\frac{\partial h}{\partial n}\cos\phi\sim\frac{\partial h}{\partial s}. \tag{5.10}$$

The contact-line equation (3.2) shows that $\cos\phi \sim \exp(-c(x-x_0))$ as $\cos\phi \rightarrow 0$. Differentiation with respect to s gives

$$\frac{\partial}{\partial s}\cos\phi \sim \cos\phi. \tag{5.11}$$

Lengthscales follow from (5.8)–(5.11):

$$s \sim 1, \tag{5.12}$$

$$n \sim Ca^{1/2}, \tag{5.13}$$

$$h \sim Ca, \tag{5.14}$$

$$\cos\phi \sim Ca^{1/2}. \tag{5.15}$$

As expected, the film thickness is an order smaller than that in the front contact region, where $h \sim Ca^{2/3}$.

These lengthscales differ from those obtained by Burgess & Foster (1990 equation (55)) for a circular flat bubble in Hele-Shaw cells. In their problem, the geometry of the circular contact line yields $\partial(\cos\phi)/\partial s \sim 1$ at the tangential-convection region. This result together with (5.8)–(5.10) gives $s \sim Ca^{1/5}$, $n \sim Ca^{2/5}$, $h \sim Ca^{4/5}$. In our case, $\partial(\cos\phi)/\partial s \sim \cos\phi$, so (5.12)–(5.14) are obtained instead.

The lengthscales of the tangential-convection region provide an estimate for the leakage rate through this region. Let $\boldsymbol{n}$ be a unit vector normal to the film boundary. From (4.6) the volume flow normal to the film boundary per unit boundary length is

$$q \equiv \boldsymbol{q}\cdot\boldsymbol{n} = \frac{1}{3Ca}h^3\frac{\partial^3 h}{\partial n^3} - h\cos\phi, \tag{5.16}$$

or

$$q \sim Ca^{3/2}. \tag{5.17}$$

Since $s \sim 1$ in the tangential-convection region, the total leakage is proportional to $qs \sim Ca^{3/2}$, which is negligible compared with the volume of film fluid ($\sim Ca^{2/3}$). Thus, the deposited film is trapped, and it subsequently rearranges to minimize surface area. This rearrangement process is studied in the next section.

6. Film rearrangement

The deposited liquid film rearranges in two stages. In the first stage, surface tension drives the film into a parabolic shape in $x \sim Ca^{-1}$. This process is studied here. In the second stage, which occurs in $x \gg Ca^{-1}$, the parabolic profile is maintained, but the film fluid leaks away through the film boundary. This leakage controlled rearrangement is studied in §7.

Film rearrangement is governed by (4.7):

$$\frac{\partial h}{\partial x} + \frac{1}{3Ca}\frac{\partial}{\partial z}\left(h^3\frac{\partial^3 h}{\partial z^3}\right) = 0. \tag{6.1a}$$

When the lengthscales $h \sim Ca^{2/3}$ and $z \sim 1$ from $h_0(z)$ are substituted into (6.1 *a*), we find $x \sim Ca^{-1}$. Thus, the first-stage film rearrangement happens in a long downstream distance compared with the width of the film. Therefore, the capillary-pressure gradient in the streamwise direction is negligible compared with that in the cross-stream direction, and is excluded in (6.1 *a*).

Boundary conditions of (6.1*a*) include the symmetry conditions at the centre of the film:

$$\frac{\partial h}{\partial z}(x, z=0) = 0, \quad \frac{\partial^3 h}{\partial z^3}(x, z=0) = 0. \tag{6.1b,c}$$

Section 5.1 shows that the film thickness is $o(Ca^{2/3})$ at the sides of the film at $z = b$, and matching gives

$$h(x, z=b) = 0. \tag{6.1d}$$

The fourth condition is that the film area is conserved,

$$\frac{\partial}{\partial x}\int_0^b h \, \mathrm{d}z = 0. \tag{6.1e}$$

The integral condition is derived as follows. Integration of (6.1*a*) yields

$$\frac{\partial}{\partial x}\int_0^b h \, \mathrm{d}z + \frac{1}{3Ca}\left[h^3 \frac{\partial^3 h}{\partial z^3}\right]_{z=b} = 0. \tag{6.2}$$

The rate of change of the film area (first term) is therefore controlled by the rate of leakage through the film boundary (second term). An order of magnitude estimate is sufficient to show that the film area is conserved for $x \sim Ca^{-1}$. The first term is $O(Ca^{5/3})$ as determined by the lengthscales $h \sim Ca^{2/3}$, $x \sim Ca^{-1}$, and $z \sim 1$. The second term requires lengthscales at the side constriction, which are determined from the following matching conditions. On one side of the constriction, the slope of the central film specifies

$$\frac{\partial h}{\partial z} \sim Ca^{2/3}. \tag{6.3}$$

On the other side, the curvature of the fluid meniscus requires (see §3),

$$\frac{\partial^2 h}{\partial z^2} \sim 1. \tag{6.4}$$

These two conditions give

$$h \sim Ca^{4/3}, \quad z \sim Ca^{2/3}. \tag{6.5}$$

Thus, the leakage rate in (6.2) is $O(Ca^{7/3})$, which is negligible compared with the first term ($\sim Ca^{5/3}$). The film area is therefore conserved in $x \sim Ca^{-1}$.

The first stage of film rearrangement is governed by (6.1). A new set of variables is defined as follows:

$$H = \frac{hb}{A_0(3Ca)^{2/3}}, \quad X = \frac{xA_0^3(3Ca)}{b^7}, \quad Z = \frac{z}{b}. \tag{6.6}$$

Substitution of these variables into (6.1) removes all parameters:

$$\frac{\partial H}{\partial X} + \frac{\partial}{\partial Z}\left(H^3 \frac{\partial^3 H}{\partial Z^3}\right) = 0, \tag{6.7a}$$

$$\frac{\partial H}{\partial Z}(X, Z=0) = 0, \quad \frac{\partial^3 H}{\partial Z^3}(X, Z=0) = 0, \tag{6.7b,c}$$

$$H(X, Z=1) = 0, \quad \int_0^1 H \, \mathrm{d}Z = 1. \tag{6.7d,e}$$

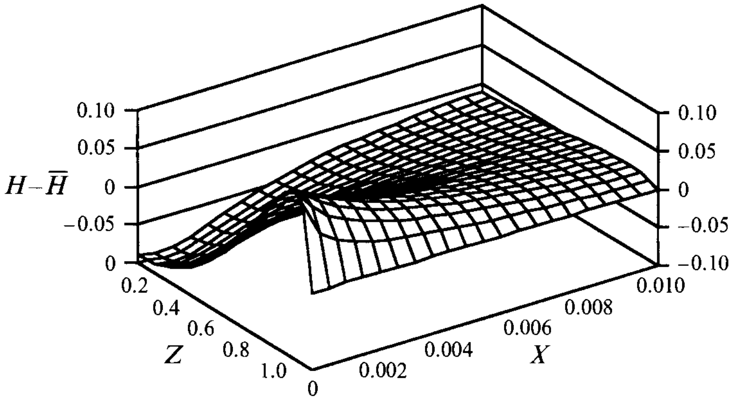

FIGURE 6. The difference between the film height, H, and the steady film height, $\bar{H}$, in a square capillary as functions of cross-stream distance Z and downstream distance X.

The initial film profile in (5.6) becomes

$$H(X=0,Z)=\frac{bk_1}{\alpha A_0}\left[1+\left(\frac{\pi}{2bc}\right)^2\tan^2\left(\frac{\pi Z}{2}\right)\right]^{-1/3} \tag{6.7f}$$

The constants b, c, α, and A_0 depend on capillary shape (table 1).

Surface-tension forces rearrange the film. Far downstream as $X \rightarrow \infty$, the film height becomes steady and is therefore independent of X. Equations (6.7*a–e*) can then be solved analytically. The steady-state solution is

$$\bar{H}=\tfrac{3}{2}(1-Z^2). \tag{6.8}$$

This parabolic profile is compared with the initial profile in figure 5. Within the small-slope approximation, a parabolic shape minimizes surface area for a given volume.

Rearrangement of fluid films from the initial to the parabolic profile is determined numerically. The integral condition (6.7*e*) slows the calculation and is avoided by transforming the dependent variable from the thickness of the film, H, to the area of the film,

$$\bar{A}(X,Z)=\int_0^Z H(X,\zeta)\,\mathrm{d}\zeta. \tag{6.9}$$

The transformed equation is solved by a backward implicit finite-difference method, which is first order in X and second order in Z. Since the equation is nonlinear, the area at each step in X is calculated iteratively by Newton's method. The numerical solution is checked under spatial and temporal refinement. Solutions presented below are computed using 1000 uniformly spaced grid points in Z and a step size of 10^{-6} in X.

Figure 6 plots the difference between the calculated film height $H(X,Z)$ and the steady profile $\bar{H}(Z)$ as functions of X and Z. Specifically, the difference along the central plane $Z=0$ is shown in figure 7(*a*). The insert shows that the difference increases first before it decays exponentially. To understand this peculiar behaviour, the steady profile is perturbed by an infinitesimal disturbance. Decomposition of the disturbance into normal modes generates a complete set of eigenfunctions (Appendix C). The initial profile is then expanded as a series of the eigenfunctions. The coefficient of the second eigenmode is found to be of opposite sign from that of the fundamental mode. Since

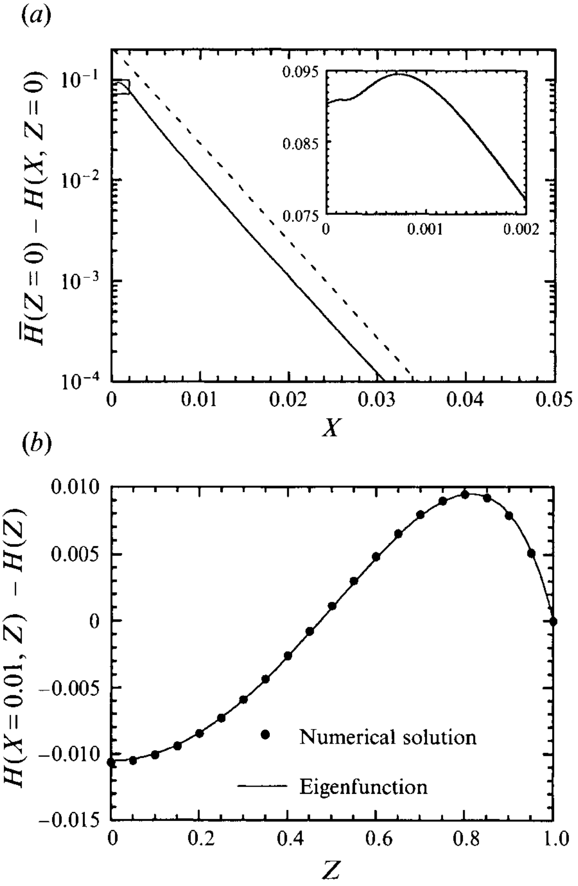

FIGURE 7. (*a*) ——, the difference between the steady film height, $\bar{H}(Z=0)$, and the computed film height, $H(X, Z=0)$, as a function of the downstream distance X. The insert expands the behaviour near $X=0$. ---, the decay of the fundamental eigenmode of an infinitesimal disturbance to the steady profile (Appendix C). (*b*) Film profiles at $X=0.01$. The steady parabolic profile is subtracted from the numerical solution. The amplitude of the fundamental eigenfunction is found by matching the film height at $Z=0$.

the second mode decays faster, the initial behaviour of the film is opposite to the late-time behaviour. The decay rate and film profile of the fundamental mode are compared with the numerical solution in figures 7(*a*) and 7(*b*). The agreement between the analytic and numerical solutions confirms that both solutions are correct.

In this section, we have obtained a numerical solution for the normalized film height $H(X, Z)$. Thus, for $X \gg 1$ to $x \sim Ca^{-1}$,

$$h(x,z) = \frac{A_0(3Ca)^{2/3}}{b} H\left(\frac{A_0^3(3Ca)x}{b^7}, \frac{z}{b}\right). \tag{6.10}$$

This solution is sufficient for determination of energy dissipation at the back end if the length of the bubble is $O(Ca^{-1})$ or less. For longer bubbles, further film rearrangement needs to be considered.

7. Second stage: thinning of the parabolic film

In the first stage ($x \sim Ca^{-1}$), film area is conserved while surface tension rearranges the film into a parabolic shape. In the second stage, leakage through the film sides becomes important, causing the film to drain. In this stage, the film remains parabolic, so only the film area needs to be determined. The solution is found to hold for all $x \gg Ca^{-1}$.

Film area A obeys (6.2):

$$\frac{\partial A}{\partial x}+\frac{1}{3Ca}\left[h^3\frac{\partial^3 h}{\partial z^3}\right]_{z=b}=0, \tag{7.1a}$$

where

$$A=\int_0^b h\,\mathrm{d}z. \tag{7.1b}$$

The second term in (7.1*a*) is the rate of leakage of film fluid through the side ($z = b$). The following analysis of the side constriction (shown as region 4 in figure 4) gives the leakage rate in terms of A. Equation (7.1*a*) can then be solved.

Flow in the side constriction satisfies (6.1*a*). Comparison of streamwise lengthscales in (6.1*a*) and (7.1*a*) shows that the flow in the constriction is quasi-steady. (This will be verified following (7.4).) Thus, (6.1*a*) simplifies to

$$\frac{h^3}{3Ca}\frac{\partial^3 h}{\partial z^3}=q, \tag{7.2a}$$

where q is the leakage rate to be determined.

Boundary conditions of (7.2*a*) are the matching conditions on either side of the constriction. Matching to the slope of the parabolic film requires

$$\frac{\partial h}{\partial z}\rightarrow-\frac{3A}{b^2}\quad \text{as } z-b\rightarrow-\infty. \tag{7.2b}$$

Matching to the curvature of the corner meniscus (§3) demands

$$\frac{\partial^2 h}{\partial z^2}\rightarrow\alpha\quad \text{as } z-b\rightarrow\infty. \tag{7.2c}$$

Lengthscales at the constriction are found from these two conditions as

$$h\sim\frac{1}{\alpha}\left(\frac{3A}{b^2}\right)^2,\quad z\sim\frac{1}{\alpha}\left(\frac{3A}{b^2}\right). \tag{7.3}$$

Substitution of these scales into (7.2*a*) gives the leakage rate

$$q=\frac{C_1}{3Ca\alpha}\left(\frac{3A}{b^2}\right)^5. \tag{7.4}$$

This equation shows how the leakage rate depends on film area. The proportionality constant $C_1 = 1.2098$ is determined by solving (7.2) numerically (Appendix D). Figure 8 shows the normalized constriction profile. An analogous leakage problem occurs in drainage of axisymmetric films (Frankel & Mysels 1962; Jones & Wilson 1978).

The quasi-steady assumption can now be verified. Given the lengthscales in (7.3), (6.1*a*) shows that the constriction evolves downstream with lengthscale $x_c \sim Ca/A^2$.

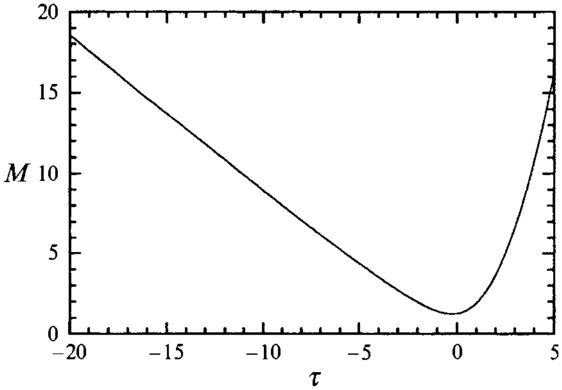

FIGURE 8. Film profile at the side constriction in $x \gg Ca^{-1}$. $M = h(3A/2b^2)^3/3qCa$ and $\tau = (z-b)(3A/2b^2)^4/3qCa$ as defined in Appendix D.

But boundary condition (7.2b) for the flow in the constriction depends on A, which varies with x as the film drains. The lengthscale (x_d) for the drainage is found from (7.1a), which requires $x_d \sim Ca/A^4$. Thus, $x_d \gg x_c$ because the maximum $A \sim Ca^{2/3} \ll 1$. Therefore, during film drainage the flow in the constriction is quasi-steady.

Substitution of (7.4) into (7.1) gives

$$\frac{\mathrm{d}A}{\mathrm{d}x}+\frac{3^5C_1}{\alpha b^{10}(3Ca)}A^5 = 0. \tag{7.5a}$$

The initial film area in (5.7) provides an initial condition,

$$A(x=0) = A_0(3Ca)^{2/3}. \tag{7.5b}$$

Thus,

$$A(x) = \frac{A_0(3Ca)^{2/3}}{[1+\beta(3Ca)^{5/3}x]^{1/4}}, \tag{7.6a}$$

where

$$\beta \equiv \frac{4(3^5)\,C_1 A_0^4}{\alpha b^{10}} \tag{7.6b}$$

is a parameter independent of Ca and x. The film profile in $x \gg Ca^{-1}$ follows directly,

$$h(x,z) = \frac{3A_0(3Ca)^{2/3}}{2b[1+\beta(3Ca)^{5/3}x]^{1/4}}\left[1-\left(\frac{z}{b}\right)^2\right]. \tag{7.7}$$

Thus, when $x \sim Ca^{-5/3}$, $h \sim Ca^{2/3}$. If $x \gg Ca^{-5/3}$, then $h \sim Ca^{1/4}x^{-1/4} \ll Ca^{2/3}$. Thus, the second stage of film rearrangement lasts indefinitely.

8. Termination of the thin film

The film terminates in the apparent contact line at the back of the bubble (i.e. region 6 in figure 4). Dissipation of mechanical energy in the termination and deposition regions determines the pressure drop needed to move the bubble. This section describes

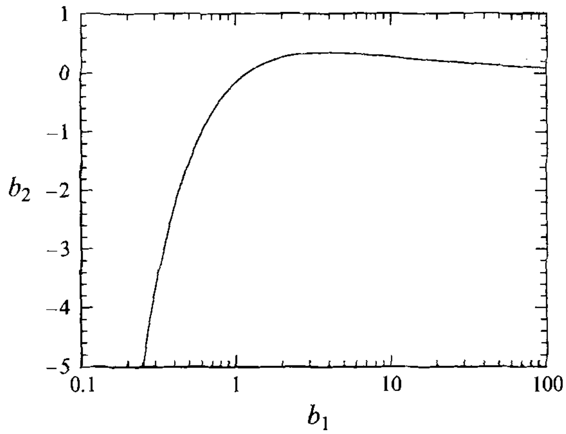

FIGURE 9. Numerical solution of b_2 *vs.* b_1.

the fluid motion in the back contact region. The result is used in Part 2 to find the pressure drop.

Film thickness in this region is governed by (5.2), with the normal component of velocity ($-\cos\phi$ in (5.2)) replaced by $\cos(\pi-\phi)$. (ϕ is defined in figure 3.) Thus,

$$\frac{\partial q}{\partial n}=0, \quad \text{where } q=\frac{1}{3Ca}h^3\frac{\partial^3 h}{\partial n^3}+h\cos(\pi-\phi). \tag{8.1a,b}$$

Let $h_1(x,z)$ be the incoming film thickness, given by (6.10) or (7.7) depending on bubble length. Then $q(s)$ is determined by the matching condition $h\rightarrow h_1$ as $n\rightarrow-\infty$. Thus, the thickness of the trailing film in the back contact region satisfies

$$\frac{\partial^3 h}{\partial n^3}=3Ca\cos(\pi-\phi)\frac{(h_1-h)}{h^3}. \tag{8.2}$$

The boundary conditions are that $h\rightarrow h_1$ as $n\rightarrow-\infty$ and $h\rightarrow\infty$ as $n\rightarrow\infty$.

Appendix B shows that the solution of (8.2) can be expressed in terms of that given by Bretherton (1961) for the trailing film in the axisymmetric flow. Here we discuss only the single property of the solution needed for determination of the drag of the bubble. The drag is the shear force exerted by the wall on the fluid films surrounding the bubble. Part 2 (equation (3.13)) gives the drag as the integral of $[h\,\partial^2 h/\partial n^2-(\partial h/\partial n)^2/2]_{n\rightarrow\infty}$ over the cross-stream width of the film. Appendix B shows that as $n\rightarrow\infty$

$$h\frac{\partial^2 h}{\partial n^2}-\frac{1}{2}\left(\frac{\partial h}{\partial n}\right)^2\rightarrow\alpha h_1 b_2. \tag{8.3}$$

α is the mean curvature of the static meniscus. b_2 is a function of $b_1\equiv\alpha h_1(3Ca)^{-2/3}\cos^{-2/3}(\pi-\phi)$. This function is obtained from a numerical solution of (8.3) (Appendix B) and is plotted in figure 9.

Figure 10 plots the product $h_1(x,z)\,b_2(x,z)$ as a function of z for two different capillaries (a square and a rectangle) and for $x\ll Ca^{-1}$, $x=Ca^{-1}$ and $x=Ca^{-5/3}$. The graph shows that the drag is of order $Ca^{2/3}$ for the bubble lengths considered. Another observation is that the curves approach zero at $z=b$, the location where tangential convection is important. This means that the tangential-convection region has negligible contribution to the drag. Thus, we omit discussion of that region here.

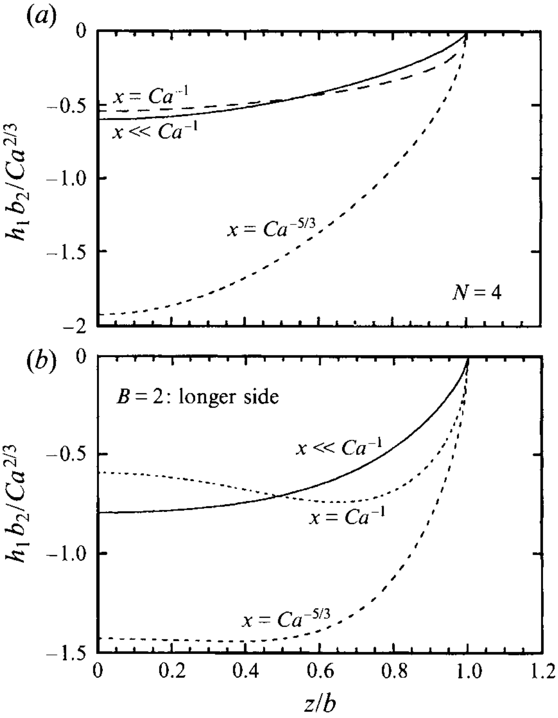

FIGURE 10. $h_1 b_2$ *vs.* z at various downstream distances x for (*a*) a square capillary with $N = 4$ and (*b*) the longer side of a rectangular capillary with aspect ratio $B = 2$.

9. Concluding remarks

This work studies the motion of long bubbles in polygonal capillaries in the limit $Ca \rightarrow 0$ to elucidate the effects of pore corners on the flow of foam bubbles in porous media. The polygonal capillaries capture the important non-axisymmetric characteristic of the pores. At the same time, they are regular enough to allow a precise calculation of the drag, pressure drop, and fluid and bubble velocities.

This first part studies the structure of the fluid films deposited by the bubble. We find that a deposited film is non-uniform in the cross-stream direction and rearranges downstream. Six film subregions have been identified, each characterized by unique lengthscales. The subregions not only reveal the physics of film deposition, rearrangement, and termination, but also allow the film profile to be expressed as a general function of the downstream distance. The film profile is used in Part 2 to calculate the drag of the bubble.

In a polygonal capillary, the pressure work is dissipated by fluid motion in the thin films and in the bulk. The dissipation in the films is strongest at the deposition and termination regions. This dissipation is found from the lengthscales in §§5 and 8 as $O(Ca^{2/3})$. In a circular capillary, the liquid and the bubble move at roughly the same speed, so the dissipation in the bulk is always an order less than that in the film. In a polygonal capillary, the liquid can bypass the bubble through the leaky corners at a velocity $\sim Ca^{-1/3} L^{-1}$, where L is the length of the bubble (Part 2). In this case, the dissipation in the bulk is $O(Ca^{1/3} L^{-1})$, which is greater than the dissipation in the films if $L \ll Ca^{-1/3}$. Under this condition, the liquid flow exhibits a new rheological response. This discovery reconciles two groups of contradictory foam flow experiments, as discussed in Part 2.

We thank a referee for correcting an error in (5.12)–(5.15). This work was partially supported by NSF Grant EAR8610494 and by the Assistant Secretary for Fossil Energy, Office of Oil, Gas, and Shale Technologies of the United States Department of Energy under Contract DE-AC03-76SF00098 to the Lawrence Berkeley Laboratory of the University of California. H.W. acknowledges fellowship support from the University of California, Berkeley during this work.

Appendix A. Explicit solutions for the mean curvature α

Because the capillary has uniform cross-section, α can be found by the following method. Consider the projection of the static meniscus onto a plane of constant x, as in figure 2. Let the area of this domain be $\mathscr{A}$ and its perimeter $\mathscr{L}$. Integration of (3.1 *a*) over this domain, followed by use of the divergence theorem shows that

$$\mathscr{L} = \alpha \mathscr{A}. \tag{A 1}$$

Both $\mathscr{L}$ and $\mathscr{A}$ can be calculated explicitly because the boundary of the projection consists of straight lines and circular arcs of radius α^{-1}. This method has been applied to menisci in non-axisymmetric capillaries with zero contact angle (Mason & Morrow 1984; Wong, Morris & Radke 1992*a*) and with finite contact angles (Wong *et al.* 1992*b*).

Given α, b is determined from the geometry of the meniscus, as shown in figure 2. For a regular polygon with N sides,

$$b = (1-\alpha^{-1})\tan(\pi/N), \tag{A 2}$$

where

$$\alpha = 1 + \left(\frac{\pi/N}{\tan(\pi/N)}\right)^{1/2}. \tag{A 3}$$

For a rectangular capillary, b and α are related differently. There are two values of b for a rectangle with aspect ratio B:

$$b = B-\alpha^{-1} \tag{A 4}$$

on the longer side with length $2B$ and

$$b = 1-\alpha^{-1} \tag{A 5}$$

on the side with length 2. Here,

$$\alpha = \frac{B+1+((B-1)^2+\pi B)^{1/2}}{2B}. \tag{A 6}$$

Values of b and α are listed in table 1.

Appendix B. Asymptotic solutions for the deposition and termination regions

At the deposition region, the governing equation (5.3) is simplified by the substitution

$$G = \frac{h}{h_0}, \quad \eta = \frac{n(3Ca\cos\phi)^{1/3}}{h_0}. \tag{B 1}$$

$$\frac{\mathrm{d}^3 G}{\mathrm{d}\eta^3} = \frac{G-1}{G^3}. \tag{B 2a}$$

The boundary conditions are the asymptotic conditions:

$$G \to 1 \quad \text{as } \eta \to -\infty, \tag{B 2b}$$

and

$$G \to \infty \quad \text{as } \eta \to \infty. \tag{B 2c}$$

As $\eta \to \infty$, (B 2) requires $\mathrm{d}^3G/\mathrm{d}\eta^3 \to 0$ or $G \to \frac{1}{2}k_1(\eta-\eta_0)^2+k_2$. $k_1 = 0.64304$ and $k_2 = 2.8996$ are obtained from a numerical solution of (B 2). η_0 merely defines the original of η and has no physical significance. Hence, as $n \to \infty$,

$$\frac{\partial^2 h}{\partial n^2} \to \frac{k_1}{h_0}(3Ca\cos\phi)^{2/3}, \tag{B 3}$$

and

$$h\frac{\partial^2 h}{\partial n^2} - \frac{1}{2}\left(\frac{\partial h}{\partial n}\right)^2 \to k_1 k_2 (3Ca\cos\phi)^{2/3}. \tag{B 4}$$

(B 3) is used in §5 to find h_0. (B 4) is used in Part 2, §3 for calculation of drag at the front of the bubble.

A numerical method has been developed for the back deposition region as described later in this Appendix. The method also applies here after minor modifications. Equation (B 2) has been solved previously by Landau & Levich (1942), Mysels, Shinoda & Frankel (1959), Bretherton (1961), Reinelt & Kraynik (1990), and Burgess & Foster (1990). However, their main focus has been the film thickness and not the drag. To calculate the drag for the back end, we find it necessary to develop our own scheme.

At the back termination region, the governing equation (8.3) is normalized by the substitution

$$G = \frac{h}{h_1}, \quad \eta = \frac{n(3Ca)^{1/3}\cos^{1/3}(\pi-\phi)}{h_1}. \tag{B 5}$$

$$\frac{\mathrm{d}^3G}{\mathrm{d}\eta^3} = \frac{1-G}{G^3}. \tag{B 6a}$$

The boundary conditions are

$$G \to 1 \quad \text{as } \eta \to -\infty, \tag{B 6b}$$

and

$$G \to \infty \quad \text{as } \eta \to \infty. \tag{B 6c}$$

Hence, as $\eta \to \infty$, $\mathrm{d}^3G/\mathrm{d}\eta^3 \to 0$ or $G \to \frac{1}{2}b_1(\eta-\eta_0)^2+b_2$. Matching to the curvature of the outer solution in (3.3) gives

$$b_1 = \frac{\alpha h_1}{(3Ca)^{2/3}\cos^{2/3}(\pi-\phi)}. \tag{B 7}$$

Once b_1 is known, b_2 is determined uniquely (see below). Thus, as $n \to \infty$,

$$h\frac{\partial^2 h}{\partial n^2} - \frac{1}{2}\left(\frac{\partial h}{\partial n}\right)^2 \to \alpha h_1 b_2. \tag{B 8}$$

This expression is needed for calculation of drag at the back end of the bubble. Given a point (x, z) on the back contact region, $h_1(x,z)$ is known from (6.10) or (7.7), and $\cos(\pi-\phi)$ ($\frac{1}{2}\pi \leqslant \phi \leqslant \pi$) from (3.2). Thus, b_1 and therefore (B 8) can be evaluated at each point along the back contact region.

The function $b_2 = b_2(b_1)$ is determined by solving (B 6) numerically. Asymptotic expansions of G in $\eta \to -\infty$ are used to initiate the integration. The solution is marched to $\eta \to \infty$ by the fourth-order Runge–Kutta method. Accurate values of b_1 and b_2 are obtained by exponentially contracting the independent variable and by using higher-order asymptotic expansions at both ends. The expansions at the negative end contain a free parameter that controls the phase angle of the exponentially growing terms (Wong 1992, p. 162). Variation of this parameter changes the values of b_1 and b_2, and generates the function $b_2 = b_2(b_1)$ plotted in figure 9.

Within $x \ll Ca^{-1}$, the film does not rearrange, i.e. $h_1(x,z) = h_0(z)$. Therefore, $b_1 = k_1 = 0.64304$ and $b_2 = -0.84529$. With film rearrangement, b_1 can take on any positive value.

Appendix C. Perturbation of the steady film area

We perturb the film area instead of the film thickness because the resulting eigenvalue problem contains a self-adjoint operator, which is very useful in proving the completeness of the eigenfunctions. Let $\delta(X, Y)$ be the disturbance to the steady film area. Thus,

$$\bar{A}(X,Z) = \int_0^Z \bar{H}(\zeta)\,\mathrm{d}\zeta + \delta(X,Z), \tag{C 1}$$

where $\bar{H}$ is the steady, parabolic film profile given in (6.8). Substitution of $\bar{A}$ into its governing equation gives, to the leading order,

$$\frac{\partial \delta}{\partial X} + \bar{H}^3 \frac{\partial^4 \delta}{\partial Z^4} = 0. \tag{C 2}$$

Separation of variables yields

$$\delta(X,Z) = \mathrm{e}^{-27\lambda X/8} g(Z), \tag{C 3}$$

where $g(Z)$ satisfies

$$(1-Z^2)^3 \frac{\mathrm{d}^4 g}{\mathrm{d}Z^4} = \lambda g. \tag{C 4a}$$

The boundary conditions in (6.7*b–e*) become

$$\frac{\mathrm{d}^2 g}{\mathrm{d}Z^2}(Z=0) = 0, \quad g(Z=0) = 0, \tag{C 4b, c}$$

$$\frac{\mathrm{d} g}{\mathrm{d}Z}(Z=1) = 0, \quad g(Z=1) = 0. \tag{C 4d, e}$$

λ is the eigenvalue to be determined together with g.

The eigenvalue problem is solved by expanding the eigenfunction $g(Z)$ in a Taylor series about the ordinary point $Z = 0$,

$$g = \sum_{i=0}^{\infty} a_i Z^i. \tag{C 5}$$

Substitution of this series into (C 4*a*) and equating the coefficient of each power of Z to zero give

$$a_{i+4} = \frac{i!}{(i+4)!}\left[\frac{3(i+2)!}{(i-2)!}a_{i+2} - \frac{3i!}{(i-4)!}a_i + \frac{(i-2)!}{(i-6)!}a_{i-2} + \lambda a_i\right],$$
$$\text{for } i = 0,1,2,\ldots, \quad \text{and} \quad a_i = 0, \quad i! = \infty \quad \text{if } i<0. \tag{C 6}$$

The convention defined in the last line compacts the representation of the coefficients. The above equation shows that a_0, a_1, a_2 and a_3 are arbitrary constants. Also, the even and odd terms are decoupled. Thus, we obtain four independent solutions of g: two even and two odd functions of Z. The boundary conditions (C 4*b*) and (C 4*c*) eliminate the two even solutions. The remaining two solutions are normalized as

$$G_1(Z;\lambda) = \sum_{\substack{i=1 \\ i\,\mathrm{odd}}}^{\infty} a_i(\lambda)\, Z^i \quad \text{with } a_1 = 1, \quad a_3 = 0, \tag{C 7a}$$

and

$$G_3(Z;\lambda) = \sum_{\substack{i=3 \\ i\,\mathrm{odd}}}^{\infty} a_i(\lambda)\, Z^i \quad \text{with } a_1 = 0, \quad a_3 = 1. \tag{C 7b}$$

Thus, any eigenfunction g must be a linear combination of these two solutions:

$$g = a_1 G_1 + a_3 G_3, \tag{C 8}$$

where a_1 and a_3 are two arbitrary constants. The boundary conditions at $Z = 1$ demand

$$g(Z=1) = a_1 G_1(1;\lambda) + a_3 G_3(1;\lambda) = 0 \tag{C 9a}$$

and

$$\frac{\mathrm{d}g}{\mathrm{d}Z}(Z=1) = a_1 \frac{\mathrm{d}G_1}{\mathrm{d}Z}(1;\lambda) + a_3 \frac{\mathrm{d}G_3}{\mathrm{d}Z}(1;\lambda) = 0. \tag{C 9b}$$

For a non-trivial solution of g, a_1 and a_3 must not be zero simultaneously. Therefore,

$$G_1(1;\lambda)\frac{\mathrm{d}G_3}{\mathrm{d}Z}(1;\lambda) - G_3(1;\lambda)\frac{\mathrm{d}G_1}{\mathrm{d}Z}(1;\lambda) = 0, \tag{C 10}$$

which determines all the eigenvalues λ_j $(j = 1, 2, 3, \ldots)$ (Wong 1992, p. 165). Specifically, $\lambda_1 = 65.526$ and $\lambda_2 = 307.22$. Hence, the slowest decay rate is given by (C 3) as $\frac{27}{8}\lambda_1$, which is plotted as a dashed line in figure 7(*a*). The eigenfunction of the fundamental mode is then obtained from (C 8). This is the eigenfunction for the film area. The corresponding film height is obtained by differentiation and is compared with the numerical solution in figure 7(*b*). The completeness of the eigenfunctions is proved following the standard procedures for eigenvalue problems with self-adjoint operators (Courant & Hilbert 1953).

Appendix D. Numerical solution for the constriction profile

The film profile is governed by (7.2), which is simplified by the substitution

$$M = \frac{h}{3Ca\,q}\left(\frac{3A}{2b^2}\right)^3, \quad \tau = \frac{(z-b)}{3Ca\,q}\left(\frac{3A}{2b^2}\right)^4, \tag{D 1}$$

$$M^3\frac{\mathrm{d}^3M}{\mathrm{d}\tau^3} = 1, \tag{D 2a}$$

$$\frac{\mathrm{d}M}{\mathrm{d}\tau} \rightarrow -1 \quad \text{as } \tau \rightarrow -\infty. \tag{D 2b}$$

$$\frac{\mathrm{d}^2M}{\mathrm{d}\tau^2} \rightarrow 3Ca\,q\alpha\left(\frac{3A}{2b^2}\right)^{-5} \quad \text{as } \tau \rightarrow \infty. \tag{D 2c}$$

As $\tau \rightarrow \infty$, $M \rightarrow \infty$, and (D 2*a*) requires $\mathrm{d}^3M/\mathrm{d}\tau^3 \rightarrow 0$ or $\mathrm{d}^2M/\mathrm{d}\tau^2 \rightarrow C_1$. The curvature C_1 is found by solving (D 2). The film height is marched from large negative τ to large positive τ by the fourth-order Runge–Kutta method. Asymptotic expansions in $\tau \rightarrow -\infty$ are used to start the integration accurately. By using an initial film height of 10, 100, or 1000, and by varying the step size from 0.02 to 0.002, the solution is found to be accurate to 10^{-9}. We find the curvature $C_1 = 1.2098$ (and the minimum height of $M = 1.2593$). The leakage rate q then follows from (D 2*c*) by equating the curvatures. This leakage problem was solved previously by Frankel & Mysels (1962) and Jones & Wilson (1978). However, their solutions for C_1 are accurate to only two significant figures.

REFERENCES

ALBRECHT, R. A. & MARSDEN, S. S. 1970 Foams as blocking agents in porous media. *Soc. Pet. Engng J.* **10**, 51.

ASSAR, G. R. & BURLEY, R. W. 1986 Hydrodynamics of foam flow in pipes, capillary tubes, and porous media. In *Encyclopedia of Fluid Mechanics* (ed. N. P. Cheremisinoff), vol. 3, chap. 2. Gulf Publishing Company, Houston, TX.

BRETHERTON, F. P. 1961 The motion of long bubbles in tubes. *J. Fluid Mech.* **10**, 166–188.

BURGESS, D. & FOSTER, M. R. 1990 Analysis of the boundary conditions for a Hele-Shaw bubble. *Phys. Fluids* A **2**, 1105–1117.

CHAMBERS, K. T. & RADKE, C. J. 1990 Capillary phenomena in foam flow through porous media. In *Interfacial Phenomena in Oil Recovery* (ed. N. R. Morrow). Marcel Dekker.

COURANT, R. & HILBERT, D. 1953 *Methods of Mathematical Physics*, vol. I, Chap. 6. Interscience.

FALLS, A. H., MUSTERS, J. J. & RATULOWSKI, J. 1989 The apparent viscosity of foams in homogeneous beadpacks. *SPE Reservoir Engng* **4**, 155–164.

FRANKEL, S. & MYSELS, K. J. 1962 On the dimpling during the approach of two interfaces. *J. Phys. Chem.* **66**, 190–191.

HIRASAKI, G. J. 1989 The steam-foam process. *J. Pet. Technol.* **41**, 449–456.

HOLM, L. W. & GARRISON, W. H. 1988 CO_2 diversion with foam in an immiscible CO_2 field project. *SPE Reservoir Engng* **3**, 112–118.

JONES, A. F. & WILSON, S. D. R. 1978 The film drainage problem in droplet coalescence. *J. Fluid Mech.* **87**, 263–288.

KOVSCEK, A. R. & RADKE, C. J. 1994 Fundamentals of foam transport in porous media. In *Foams: Fundamentals and Applications* (ed. L. L. Schramm), vol. 242, pp. 115–163. Washington, DC. American Chemical Society.

LANDAU, L. & LEVICH, B. 1942 Dragging of a liquid by a moving plate. *Acta Physicochimica URSS* **17**, 42–54.

MASON, G. & MORROW, N. R. 1984 Meniscus curvatures in capillaries of uniform cross-section. *J. Chem. Soc. Faraday Trans.* **80**, 2375–2393.

MYSELS, K. J., SHINODA, K. & FRANKEL, S. 1959 *Soap Films: Studies of their Thinning and a Bibliography*. Pergamon.

PARK, C. W. & HOMSY, G. M. 1984 Two-phase displacement in Hele-Shaw cells: theory. *J. Fluid Mech.* **139**, 291–308.

REINELT, D. A. 1987 The effect of thin film variations and transverse curvature on the shape of fingers in a Hele-Shaw cell. *Phys. Fluids* **30**, 2617–2623.

REINELT, D. A. & KRAYNIK, A. M. 1990 On the shearing flow of foams and concentrated emulsions. *J. Fluid Mech.* **215**, 431–455.

SAFFMAN, P. G. & TAYLOR, G. I. 1958 The penetration of a fluid into a porous medium or Hele-Shaw cell containing a more viscous liquid. *Proc. R. Soc. Lond. A* **245**, 312–329.

SCHWARTZ, L. W., PRINCEN, H. M. & KISS, A. D. 1986 On the motion of bubbles in capillary tubes. *J. Fluid Mech.* **172**, 259–275.

STEBE, K. J., LIN, S. Y. & MALDARELLI, C. 1991 Remobilizing surfactant retarded fluid particle interfaces. I. Stress-free conditions at the interfaces of micellar solutions of surfactants with fast sorption kinetics. *Phys. Fluids* A **3**, 3–20.

WEATHERBURN, C. E. 1938 *An Introduction to Riemannian Geometry and the Tensor Calculus.* Cambridge University Press.

WONG, H. 1992 The motion of a long bubble in polygonal capillaries at low capillary numbers. PhD thesis, University of California, Berkeley.

WONG, H., MORRIS, S. & RADKE, C. J. 1992*a* Two-dimensional menisci in non-axisymmetric capillaries. *J. Colloid Interface Sci.* **148**, 284–287.

WONG, H., MORRIS, S. & RADKE, C. J. 1992*b* Three-dimensional menisci in polygonal capillaries. *J. Colloid Interface Sci.* **148**, 317–336.

WONG, H., RADKE, C. J. & MORRIS, S. 1995 The motion of long bubbles in polygonal capillaries. Part 2. Drag, fluid pressure and fluid flow. *J. Fluid Mech.* **292**, 95–110.